This is a preprint, the final version is subject to change, of the American Mineralogist (MSA)
Cite as Authors (Year) Title. American Mineralogist, in press.
DOI: https://doi.org/10.2138/am-2020-7060

Revision 1

Equations of state, phase relations, and oxygen fugacity of the Ru-RuO_2 buffer at high pressures and temperatures

Katherine Armstrong[1*], Nicki C. Siersch[1], Tiziana Boffa-Ballaran[1], Daniel J. Frost[1], Tony Yu[2], and Yanbin Wang[2]

1- Bayerisches Geoinstitut, Univeristy of Bayreuth, Universität Str. 30 95447, Bayreuth, Germany
2- GSECARS, University of Chicago, Building 434A, Argonne National Laboratory, 9700 South Cass Ave. Lemont, IL 60439 USA

*Now at Peter A. Rock Thermochemistry Laboratory, University of California Davis, 1 Shields Ave, 4415 Chemistry Annex, Davis, CA, 95616 USA

Abstract

Experimental studies and measurements of inclusions in diamonds show that ferric iron components are increasingly stabilized with depth in the mantle. To determine the thermodynamic stability of such components their concentration needs to be measured at known oxygen fugacities. The metal-oxide pair Ru and RuO_2 is ideal as an internal oxygen fugacity buffer in high pressure experiments. Both phases remain solid to high temperatures and react minimally with silicates, only exchanging oxygen. To calculate oxygen fugacities at high pressure and temperature, however, requires information on the phase relations and equation of state properties of the solid phases.

We have made in situ synchrotron X-ray diffraction measurements in a multianvil press on mixtures of Ru and RuO_2 to 19.4 GPa and 1473 K, with which we have determined phase relations of the RuO_2 phases and derived thermal equations of state (EoS) parameters for both Ru and RuO_2. Rutile-structured RuO_2 was found to undergo two phase transformations, first at approximately 7 GPa to an orthorhombic structure and then above 12 GPa to a cubic structure. The phase boundary of the cubic phase was constrained for the first time at high pressure and temperature. We have derived a continuous Gibbs free energy expression for the tetragonal and orthorhombic phases of RuO_2 by fitting the second-order phase transition

boundary and P-V-T data for both phases, using a model based on Landau theory. The transition between the orthorhombic and cubic phases was then used along with EoS terms derived for both phases to determine a Gibbs free energy expression for the cubic phase. We have used these data to calculate the oxygen fugacity of the Ru + O_2 = RuO_2 equilibrium, which we have parameterised as a single polynomial across the stability fields of all three phases of RuO_2. The expression is: $\log_{10} f_{O2}\,(\text{Ru-RuO}_2) = (7.782 - 0.00996P + 0.001932P^2 - 3.76 \times 10^{-5}P^3) + (-13763 + 592P - 3.955P^2)/T + (-1.05\text{x}10^6 - 4622P)/T^2$, which should be valid from room pressure up to 25 GPa and 773-2500 K, with an estimated uncertainty of 0.2 log units. Our calculated f_{O2} is shown to be up to 1 log unit lower than estimates that use previous expressions or ignore EoS terms.

Introduction

Knowledge of the redox conditions, or more specifically the oxygen fugacity (f_{O_2}), at which rocks and melts formed is important for understanding a host of phenomena, such as the partitioning of variably valent elements, the speciation of volatiles, and the formation of accessory phases like sulfides, diamond, and metal alloys (Hirschmann et al. 2012; Gaillard et al. 2015; Smith et al. 2016; Davis and Cottrell 2018). Perhaps most importantly, the f_{O_2} of the mantle has controlled the nature of volcanically degassed species throughout Earth's history (Hirschmann 2012). In addition, mantle f_{O_2} influences transport properties such as diffusion, creep, and electrical conductivity by controlling the Fe^{3+}/Fe^{2+} ratio and OH^- contents of minerals and melts (e.g., Pommier et al. 2010; Keefner et al. 2011; Yoshino and Katsura 2013). In order to place quantitative constraints on the effects of any redox or redox-influenced process at mantle conditions, experimental studies that either control or measure the f_{O_2} are necessary.

Recent studies on the speciation of ferric iron in minerals and melts at high pressure have further indicated the need for quite specific controls on oxygen fugacity (Tao et al. 2018; Zhang et al. 2017). Although the concentration of ferric iron in upper mantle rocks is relatively low (Canil and O'Neill 1996; Woodland et al. 2006), studies of sublithospheric diamonds (Kiseeva et al. 2018) and experimental studies at transition zone and lower mantle conditions indicate that the ferric iron components of minerals are increasingly stabilized with depth in the mantle (Lauterbach et al. 2000; Rohrbach et al. 2007). In order to explore this tendency, it is important to be able to determine the chemical potentials of ferric iron-bearing components in minerals and melts. One way to do this is to fix the oxygen fugacity of

an experiment at conditions where measurable amounts of ferric iron components are present, and then determining their concentration (O'Neill et al. 2006).

Standard methods that use redox buffering assemblages to fix fO_2 in experiments face major challenges when applied at pressures consistent with the deep mantle. They require too much space in the experimental apparatus to be practical, and uncertainties arise in both the activities and standard state properties of the components involved. The use of an outer capsule containing an H_2O-saturated redox buffer (Eugster 1957), for example, is problematic above 3 GPa because the solute content of the fluid makes it difficult to determine the activity of H_2O in the inner capsule, which is required to calculate the fO_2 (Matjuschkin et al. 2015). Noble metal redox sensors can be used to determine the fO_2 of iron-bearing assemblages (Woodland and O'Neill 1997), however, at pressures above 15 GPa, uncertainties in the effect of pressure on the excess molar volumes of the alloy solid solutions contribute to very large errors in calculated fO_2 (Stagno et al. 2011).

One solution is to use pure solid buffering assemblages inside the experimental capsule. This allows the buffer to be in close proximity to the sample, which ensures that they can equilibrate directly. The best buffers for this purpose are those that undergo minimal chemical interaction with the sample under investigation, other than exchanging oxygen, such as $Re + O_2 = ReO_2$ and $Ru + O_2 = RuO_2$ (Smyth et al. 2014; Righter et al. 2004). At the other end of the scale, Fe metal is similarly effective at rendering an fO_2 close to the iron-wüstite (IW; $2Fe + O_2 = 2FeO$) buffer, although the chemical potential of at least one coexisting ferrous iron phase is required (Rohrbach et al. 2007). The direct mixing of buffers into assemblages is probably the most reliable method for fixing and calculating oxygen fugacities of sufficient accuracy to determine the chemical potentials of ferric iron components at pressures compatible with the deep mantle. However, the thermal equations of state and phase relations of the buffering assemblage need to be accurately known.

A metal-oxide fO_2 buffer has the form

$$\mathrm{M} + \left(\frac{x}{4}\right) * \mathrm{O}_2 = \mathrm{MO}_{(x/2)} \tag{1}$$

where M is a metal and x is its valence state in the oxide. As long as both solid phases are pure, the oxygen fugacity can be calculated from:

$$\frac{x}{4} * RT \ln fO_2 = \Delta_r G^o_{(T,1\text{bar})} + \int_{1\text{bar}}^{P} \Delta V dP \quad (2)$$

where R is the universal gas constant, T is temperature, $\Delta_r G^o_{(T,1\text{bar})}$ is the standard-state Gibbs free energy of the equilibrium at ambient pressure and at the temperature of interest, and ΔV is the volume change of the solid phases. As the pressure increases, the accuracy to which ΔV needs to be determined also increases. Above 10 GPa, thermal equations of state (EoS) for the metal and oxide phases at conditions close to those of interest are required to reduce the uncertainties. Potentially of even greater importance, the phases of the buffering assemblage may undergo phase transitions at high pressures and/or temperatures. If so, the thermodynamic properties of these phases are also required to calculate the fO_2.

Campbell et al. (2009) used synchrotron X-ray diffraction to determine the thermal EoS for the metal-oxide pairs Fe-FeO and Ni-NiO in a multi-anvil press and laser-heated diamond anvil cells, to 80 GPa and 2500 K (Campbell et al. 2009). These data were then used to calculate the fO_2 of the Fe-FeO and Ni-NiO buffers over this range of conditions, which are to date the only buffering assemblages that are accurately calibrated to lower mantle settings. By determining the EoS of both metal and oxide in a single experiment, the properties become internally consistent and the absolute errors affecting both phases cancel to some degree when the buffering equilibrium is used to calculate oxygen fugacity.

Here we report synchrotron X-ray diffraction data on an assemblage of Ru and RuO_2 collected to pressures of 18.2 GPa and temperatures up to 1473 K in a multi-anvil press. This assemblage has particular advantages for buffering the fO_2 of silicate melts in order to examine the pressure effect on melt ferric/ferrous ratios (O'Neill and Nell 1997; O'Neill et al. 2006; Zhang et al. 2017). Both metal and oxide undergo minimal reaction with coexisting silicate melts, therefore they can be mixed directly with the melt phase or silicate minerals. Ruthenium also has a relatively low solubility in silicate melts. In addition, as the buffered fO_2 is relatively high, Fe loss into Pt capsules is not significant and ferric Fe is present in sufficient concentrations to be accurately measured.

Thermal expansion data at room pressure are available for both Ru and RuO_2, and compression studies at room temperature have been performed (Clendenen and Drickamer 1964; Rao and Iyengar 1969; Schroeder et al. 1972; Hazen and Finger 1981), however, no volume data at simultaneous high pressures and temperature are available. More importantly,

RuO_2, which has a tetragonal rutile-type structure at room pressure, undergoes a series of phase transformations with increasing pressure. At room temperature, a second-order ferroelastic phase transformation to an orthorhombic $CaCl_2$-type structure has been observed above 7 GPa (Haines and Léger 1993; Rosenblum et al. 1997; Ono and Mibe 2011). Further, a cubic pyrite-type structure has been observed above 11 GPa (Haines and Léger 1993), which has also been synthesised and recovered from 20 GPa and 1373 K (Haines et al. 1998). For the first time we have determined the thermal EoS properties of these phases simultaneously at high-pressures and high-temperature and we have constrained their phase relations in order to use the Ru-RuO_2 buffer at conditions compatible with the transition zone of the mantle.

Experimental Methods

In situ high-pressure high-temperature experiments

Samples of reagent-grade Ru metal and RuO_2 powders were mixed together in the ratio 30:70 by weight, respectively, and cold pressed into pellets 1.7 mm in diameter and 1 mm thick. Pellets of the same size were also prepared of MgO mixed with Au powder in the ratio 90:10 for use as a pressure calibrant. Pellets of both were loaded into a 10-mm edge-length Cr-doped MgO octahedral pressure medium inside an MgO sleeve, separated by thin (0.3 mm) Al_2O_3 spacers of the same diameter. Solid polycrystalline MgO filled the space above and below the samples and calibrant. A 25 μm thick rhenium foil furnace was used to heat the sample, with laser cut windows to allow for X-ray diffraction measurements. The furnace was surrounded by a ZrO_2 sleeve to provide thermal insulation. Temperature was monitored by a $W_{97}Re$-$W_{75}Re$ (type D) thermocouple, inserted normal to the X-ray beam with the foil furnace serving as the high-T junction (Fig. 1).

The assembly was compressed with high-hardness Fujilloy TF05 tungsten carbide (WC) anvils with 4-mm edge-length truncated corners (Ishii 2016) in the large volume press installed at beamline 13-ID-D at the Advanced Photon Source, Argonne National Laboratory (e.g. Wang et al. 2009; Chantel et al. 2012). Energy dispersive X-ray diffraction data from the sample and the pressure calibrants were collected using a Ge solid state detector at a diffraction angle of 6.1°, calibrated at room pressure using the diffraction patterns of Au and MgO. A YAG phosphor crystal was placed in the beam path behind the sample to convert the

X-ray absorption contrast of the assembly into visible light. A charge-coupled device (CCD) was used to record images of the sample assemblage in order to focus the diffraction beam either on the Ru-RuO_2 pellets or on the Au-MgO mixture through the windows cut into the Re furnace (Fig. 2), and to avoid in this way interference from the assemblage materials.

Two experiments were performed, with each experiment comprising three to four temperature cycles. For each cycle, pressure was first increased to a target value, followed by heating to a peak temperature. X-ray diffraction measurements were then performed on both the sample and the pressure calibrant materials as the temperature was dropped in steps of 200 K to 773 K and then in one step to room temperature. The assembly was then compressed further at room temperature and the temperature was again raised for another cycle (Fig. 3). The peak temperature was 1273 K for the first experiment and 1473 for the second. During heating at constant load, sample pressure generally increased slightly, whereas it dropped during cooling. The only exception to this was during the first heating cycle of each experiment. In the case of the first experiment (T2135) the small drop in pressure was likely due to the different thermal expansions of the materials of the cell assembly, whereas in the case of the second experiment (T2140), the pressure was observed to drop significantly during heating, most likely due to the formation of cubic RuO_2 and the consequent large volume change associated with the transition (Fig. 3).

Unit-cell parameters for MgO, Au, Ru and RuO_2 at each pressure and temperature were obtained by fitting the collected energy dispersive powder X-ray diffraction patterns using the full profile LeBail method implemented in the GSAS software package included in the EXPGUI interface (Larson and Von Dreele 2004; Toby 2001). This method is based on the principal that the diffraction pattern is made up as a sum of the different phases included in the investigated sample, therefore it is particularly suitable for resolving overlapping diffraction peaks. The unit-cell lattice parameters of Au and MgO were used to determine the pressure conditions of the experiment employing the *P-V-T* equations of state of Tsuchiya (2003) and Dewaele et al. (2000), respectively (Table 1). In general there was good agreement between the pressure values calculated using the two different calibrants; the values obtained from the unit-cell lattice parameter of Au were taken to be more reliable, however, as many of the assembly component parts are MgO and interference of the diffraction lines from MgO that was not within the furnace hot spot could not be excluded. The resulting unit-cell lattice parameters determined at the different *P-T* conditions for Ru and RuO_2 are reported in Tables 2 and 3, respectively.

Quench experiments

A series of quench experiments were performed at the Bayerisches Geoinstitut using 18 mm and 10 mm edge-length octahedral assemblies of very similar design as described above, but with $LaCrO_3$ furnaces. These assemblies were employed with WC anvils of either 8 mm truncations in a 5000 tonne press or 4 mm truncations in a 1200 tonne press, respectively. Ru and RuO_2 mixtures were employed as a buffering assemblage inside platinum capsules. After the experiments were quenched, the recovered RuO_2 phase was identified using either X-ray powder diffraction or Raman spectroscopy by comparison with spectra previously reported (Haines et al. 1998; Rosenblum et al. 1997). The RuO_2 phases determined for these quench experiments are reported in Table 4 together with the corresponding pressure and temperature conditions of the multi-anvil runs. The pressure conditions of the multi-anvil runs were estimated from previous calibrations (Frost et al. 2004) with an uncertainty of approximately 0.5 GPa, whereas temperatures were monitored with D type thermocouples with a temperature uncertainty of the order of 100 K.

Results

Examples of full profile Le Bail fitting of energy dispersive diffraction patterns collected at different pressures and temperatures are shown in Figure 4. Fluorescence peaks in the range between 85 and 88 keV have been ignored during the analysis. The unit-cell volume (V) data of Ru and RuO_2 obtained at different pressures and at room temperature were fitted using a modified Tait EoS (Holland and Powell 2011; Huang and Chow 2002), implemented in the EoSFit7 software (Angel et al. 2014). This EoS was employed because it is easily invertible and, therefore, more amenable for ultimately calculating the fo_2. The room pressure unit-cell volume V_0 and the room pressure bulk modulus K_0 were simultaneously refined, whereas the first pressure derivative of the bulk modulus, K_0', was fixed to the value of 4.

Two methods were used to fit the high-pressure and high- temperature data. In the first, the room pressure volume is described with the following thermal expansion expression:

$$\mathrm{V}_T = \mathrm{V}_0 \exp\left[\int_{T_0}^{T} \alpha dT\right] \tag{3}$$

and the effect of temperature on the bulk modulus is described by:

$$K_T = K_0 + (\partial K_T/\partial T)_P (T - T_0) \tag{4}$$

where α is the volumetric coefficient of thermal expansion, here approximated with a linear function $\alpha(T) = \alpha_0 + \alpha_1 T$. Using this approach, $\partial K_T/\partial T$, α_0, and α_1 are simultaneously refined. In the second approach, an expression for thermal pressure was used in conjunction with an isothermal EoS. The thermal pressure term is defined as:

$$P_{\text{th}} = \int_{T_0}^{T} \alpha K dT \,|_V \tag{5}$$

The function αK is assumed to have the form of a heat capacity curve; i.e., becoming constant at high temperature and decreasing to zero at 0 K, and so is modelled with an Einstein function:

$$\xi = \left(\frac{\alpha_0 K_0}{\xi_0}\right) \frac{u^2 e^u}{(e^u - 1)^2} \tag{6}$$

where α_0, K_0, and ξ_0 are the values at ambient conditions, $u = \theta/T$, and θ is the Einstein temperature. An approximate value for θ can be estimated for each phase via the relation $\theta = 10636/(S/n + 6.44)$, where S is the molar entropy (in J K^{-1} mol^{-1}) and n is the number of atoms per formula unit (Holland & Powell 2011). P_{th} then can be rewritten as:

$$P_{\text{th}} = \int_{T_0}^{T} \alpha_0 K_0 \frac{\xi}{\xi_0} dT = \alpha_0 K_0 \frac{\theta}{\xi_0} \left(\frac{1}{e^u - 1} - \frac{1}{e^{u_0} - 1}\right) \tag{7}$$

In this approach only α_0 is a refinement parameter. This EoS contains an implicit thermal effect on the compressibility. Both thermal models also are implemented in the Eosfit7 program (Angel et al. 2014).

P-V-T **data and equation of state for ruthenium metal**

Ruthenium metal has a hexagonal (hcp) unit cell with space group $P6_3/mmc$ ($Z = 2$). The unit-cell volumes collected in the two different experiments (Table 2) have been normalized with respect to their room pressure values and are reported in Figure 5, normalised to $V_0 = 27.185$ Å^3. No structural transitions were observed up to the maximum pressure and temperature conditions reached. The normalized data were fitted together with the room pressure thermal expansion data from Schroeder et al. (1972), which extend to 2000 K in

order to constrain the *P-V-T* EoS parameters for this material. Although the Einstein thermal pressure model has been shown to successfully describe data on silicate minerals (Holland and Powell 2011), it was found to be insufficiently flexible to fit the high-temperature data of Schroeder et al. (1972). Thus, for Ru metal, the polynomial thermal expansion model was used to fit the high-temperature data both at room and at high pressure, whereas the modified Tait EoS, with K' fixed to the value of 4, was used for the room temperature data. The resulting *P-V-T* parameters are reported in Table 5. The values of K_0 obtained from the Tait EoS fitting (304 ± 2 GPa) is identical within uncertainties to the bulk modulus obtained for fitting the data using a second order Birch-Murnaghan EoS.

Clendenen and Drickamer (1964) reported lattice parameters for Ru from room temperature compression experiments up to 40 GPa and their data also are reported in Figure 5 with $V_0 = 27.185$ Å^3. There is an excellent agreement between the two sets of data. More recent density functional theory calculations on Ru by Lugovskoy et al. (2014) yield a K_0 = 332.5 GPa at 0 K, which is also in reasonable agreement with our result.

Ruthenium oxide phase relations and *P-V-T* equations of state

At ambient conditions, RuO_2 has a tetragonal space group ($P4_2/mnm$, Z = 2) with a rutile-type structure. As this is isostructural with SiO_2 stishovite, there have been significant previous experimental and ab initio studies aimed at characterizing its structure and phase transformations as a possible analogue for SiO_2 in the lower mantle. RuO_2 has been found to undergo two phase transitions with pressure. At room temperature it first undergoes a second-order ferroelastic phase transformation above 7 GPa, to an orthorhombic $CaCl_2$-type structure with space group *Pnnm* (Z = 2). At pressures above 12 GPa at room temperature, evidence for a first-order phase transition has been observed to a cubic pyrite-type (or modified fluorite) structure with space group $Pa\bar{3}$ (Z = 4) (Haines et al. 1996; 1997; 1998; Haines and Léger 1993; Ming and Magnhani 1982; Ono and Mibe 2011; Ahuja 2001; Rosenblum et al. 1997). All three phases were encountered in this study (Table 3) and the variations with pressure and temperature of their molar volumes are shown in Figure 6.

In our experiments, the transition from the tetragonal to orthorhombic structure was found to occur between 7.5 and 9.8 GPa at ambient temperature (Figs. 6 and 7). Several previous studies have determined the transition pressure associated with the tetragonal to orthorhombic transformation. Using X-ray powder diffraction in a diamond anvil cell Haines

and Léger (1993) report observation of the $CaCl_2$-type phase at 8 GPa and proposed, based on a back-extrapolation of the unit cell parameters, that the phase transition occurred at 5 GPa. A subsequent study with neutron diffraction (Haines et al., 1997) found the transition at 5.3 GPa, although pressure was determined using the equation of state of the tetragonal RuO_2 phase itself, reported by Hazen and Finger (1981). Rosenblum et al. (1997) used Raman spectroscopy in a diamond anvil cell and splitting of the E_g mode to determine a transition pressure of 11.8 GPa, while Ono and Mibe (2011) used essentially the same methodology to determine a transition at 7.6 GPa, which is in very good agreement with our result. Ono and Mibe (2011) discuss a number of possible explanations for the difference in pressure of the transition compared to the study of Rosenblum et al. (1997), however, we note that both our result and the result of Ono and Mibe (2011) have the advantage that the samples were heated between measurements, which should reduce differential stresses that might influence the transition. This result also is in good agreement with the ab initio value of 8 GPa (Gupta and Jha, 2014), and lower than the 9 GPa determined by Tse et al. (2000). The slope of the phase boundary determined from our experiments differs only very slightly from that of Ono and Mibe (Fig. 7) and is quite tightly constrained by both data sets. The results of higher-temperature quench experiments that contained mixtures of Ru and RuO_2 are also shown in Figure 7. Although information on the orthorhombic phase would not be preserved in these recovered experiments, the phase boundaries determined imply that the orthorhombic phase is barely stable at these high temperatures.

To determine the *P-V-T* EoS of the tetragonal phase, we also included the room temperature single-crystal compression data from Hazen and Finger (1981) up to 2.8 GPa, which are in excellent agreement with our room temperature tetragonal data (Fig. 6), and the room-pressure thermal expansion data from Rao and Iyengar (1969) up to 975 K. The resulting EoS parameters, obtained using a modified Tait EoS with $K' = 4$ for the room temperature high-pressure data and the expression for thermal pressure for the high temperature data, are reported in Table 5. The bulk modulus of 261 ± 4 GPa is in reasonable agreement with the ab initio calculations of Tse et al. (2000), who, depending on the density gradient corrections employed, obtained either 299 or 249 GPa, with $K' \sim 4$. The thermal expansion coefficient (α_0) obtained, $1.57 \cdot 10^{-5}$ K^{-1}, is very similar to that of stishovite (Ito et al., 1974). Interestingly, the unit-cell *c*-axis of the RuO_2 tetragonal phase shows a negative thermal expansion at room pressure (Rao and Iyengar, 1969), which is preserved in our high-pressure data and also appears to be maintained in the unit-cell *c*-axis of the orthorhombic

phase. This may result from the rotation of octahedra during heating giving rise to a geometrical shortening of the *c*-axis in spite of the octahedral expansion.

It is clear that a significant softening of the structure occurs upon the second-order phase transition to the orthorhombic phase (Figure 6). If we were to fit the available data for the orthorhombic phase to a separate EoS the bulk modulus would be ~ 110 GPa. However, given the paucity of the volume data and the fact that we expect the elastic properties to change rapidly in the region of such a transition, a more reasonable approach is to adopt the description of ferroelastic phase transitions within the framework of Landau theory, which defines an excess Gibbs free energy term ($G_{P,T}^{ex}$) to describe the energetic consequences of a transition. The advantage of this approach is that both the phase relations and the relationship between the volumes of the two phases can be described through a single $G_{P,T}^{ex}$ expression. This provides internal consistency through a relatively small number of adjustable parameters. The high-symmetry tetragonal phase is considered to form above a critical temperature, T_c, which is anchored at room pressure at the value T_c^0. Following Holland and Powell (1998), and a lack of evidence to the contrary, we assume that T_c is linear with pressure and that the slope of the transition is related to the maximum volume (V_{max}) and entropy (S_{max}) encountered during the transition, i.e.:

$$\frac{dT_c}{dP} = \frac{V_{max}}{S_{max}} \tag{8}$$

The phase relations can, therefore, be fitted to the expression,

$$T_c = T_c^0 + \frac{V_{max}}{S_{max}} P \tag{9}$$

The volume at pressure and temperature is described by

$$V_{P,T} = V_{P,T}^0 + V_{P,T}^{ex} \tag{10}$$

where $V_{P,T}^0$ is the volume of the tetragonal phase excluding any contribution from the phase transition, as explained later. $V_{P,T}^0$ can be determined using the *P*-*V*-*T* EoS methods previously described. $V_{P,T}^{ex}$ is the excess volume arising from the transition. In Landau theory the excess properties vary across the phase transition as a function of an order parameter, Q. The rutile to $CaCl_2$-type transition ($P4_2/mnm \leftrightarrow Pnnm$) in RuO_2 and SiO_2 stishovite is second-order (Haines and Léger 1993; Carpenter et al. 2000), such that the temperature dependence of the order parameter is given by:

$$Q^2 = (1 - \frac{T}{T_c}) \tag{11}$$

Higher order terms of Q (Carpenter et al. 2000) are neglected, as their influence on the volume and $G_{P,T}^{ex}$ would be relatively minor and we are not attempting to model the elastic behavior. The excess volume is then calculated as

$$V_{P,T}^{ex} = V_{max}(Q_{298}^2 - Q^2) \tag{12}$$

where Q_{298} is the value of the order parameter at the reference temperature of 298 K. Q is set to 0 in the tetragonal stability field, i.e. where $T > T_c$, $V_{P,T}^{ex}$ then becomes equal to $V_{max}Q_{298}^2$. Consequently, the volume in the tetragonal field also contains a contribution from $V_{P,T}^{ex}$ and $V_{1bar,298}^{o}$ must be corrected for this (Carpenter et al. 2000; Angel et al. 2017). $V_{1bar,298}^{0}$ is, therefore, smaller than the measured volume of the tetragonal phase at ambient conditions by $\sim V_{max}$.

We can determine values of $V_{1bar,298}^{0}$, V_{max}, S_{max}, and T_c^0 by fitting both the experimental phase transition conditions using the data in Figure 7 and the volume data for the orthorhombic phase simultaneously (Fig. 6), however, to make the fitting internally consistent for both phases we also refine K_0 and α_0 of the tetragonal phase in a weighted least squares refinement. The resulting parameters are reported in Table 5. The refined phase transition boundary is shown in Figure 7, and the volumes predicted by the model along different isotherms are shown in Figure 6. The refined gradient of the phase boundary is 223 K GPa^{-1}. This is at the high end of the values proposed for the isostructural SiO_2 stishovite to $CaCl_2$-type structure transition, which range from 180 to 64.6 K GPa^{-1} (Akins and Ahrens 2002; Fischer et al. 2018 and references therein). This value is, however, in very good agreement with several ab initio determinations for the slope of the SiO_2 transition boundary (Tsuchiya et al. 2004; Yang and Wu 2014). As shown in Figure 6, the volumes are predicted to drop rapidly with pressure as the phase transition is crossed, but this effect gets smaller at higher temperatures. If such behavior also occurs during the isostructural stishovite to $CaCl_2$-type structure transition in SiO_2, we can expect a similar reduction in the extent of volume softening due to the transition at high temperatures.

The cubic RuO_2 phase was formed on heating to 1473 K at 15.8 GPa. Although the observations are not reversed, cooling of the cubic phase to 1273 K at 15 GPa and 1073 K at 14.1 GPa resulted in no back transformation and we tentatively assume that the cubic phase

remained in its stability field at these conditions. Furthermore, an experiment at 13.7 and 1073 K remained in the orthorhombic structure, providing a tight bracket on the transition conditions at this temperature. Multi-anvil quench experiments at 2473 K that produced the tetragonal and cubic phases at 17 GPa and 20 GPa, respectively, also constrain the transformation boundary, which is fitted with a thermodynamic model described in the next section. If the resulting boundary, shown in Figure 7, is extrapolated to room temperature, the orthorhombic to cubic transition pressure is ~ 11.5 GPa. This is in good agreement with the appearance of X-ray diffraction lines for the cubic phase that were observed above 12 GPa at room temperature by Haines and Léger (1993), who found this to be a kinetically slow transition, with some crystals still in the orthorhombic structure to 40 GPa. Both the cubic and the orthorhombic phases must have the potential to remain metastable at temperatures below 1073 K, however, as Ono and Mibe (2011) report the occurrence of the orthorhombic phase at pressures where our reaction boundary would imply that the cubic phase is stable. For this reason we did not employ data below 1073 K to constrain the stability field of the cubic phase, as the potential for metstability exists. Ab initio simulations (Tse et al. 2000) predict the room temperature orthorhombic to cubic transition at a slightly greater pressure of 13 GPa.

The *P-V-T* EoS of the cubic phase was fitted using the data shown in Figure 6. This yields a significantly lower bulk modulus (269 ± 12 GPa) than previously proposed (399 GPa, Haines and Léger, 1993). Ab initio studies have predicted lower values of the bulk modulus, between 299 and 380 depending on method (Lundin et al. 1998; Tse et al. 2000), with the lowest calculated value still greater than our refined value. It is possible that the sparse data coverage provides insufficient constraints on K_0, particularly if K_0' for this phase is different to 4. Note, however, that the V_0 obtained from the EoS fit is in good agreement with the room pressure unit-cell volume (114.73 ± 2 Å^3) measured for the Ru/RuO_2 sample recovered from experiment T2140. As the objective of this work is to facilitate calculating the Gibbs free energy of RuO_2 phases at high *P* and *T*, finding fit parameters that accurately describe the elastic properties is a secondary concern to deriving a model that suitably describes the volumes at pressures and temperatures conditions of interest. As will be shown, large uncertainties in K_0 for cubic RuO_2 result in relatively small uncertainties in the calculated fo_2 for the Ru-RuO_2 buffering equilibrium. Our data indicate a ΔV of the orthorhombic-cubic transition at room temperature to be 7.3% at the approximate pressure of

the transition. This is between the previously reported values of 6.1% (Haines et al. 1996) and 10% (Ming and Magnhani 1982).

Thermodynamic analysis of the RuO_2 phase relations

In order to calculate oxygen fugacities for the Ru-RuO_2 buffer, descriptions for the Gibbs free energies of all three RuO_2 phases are required. The Gibbs free energy for both tetragonal and orthorhombic phases can be determined from the Landau theory expression:

$$G_{P,T}^{Tet/Orth} = G_{P,T}^{o} + G_{P,T}^{ex} \tag{13}$$

where $G_{P,T}^{o}$ is the Gibbs free energy of the high-symmetry tetragonal phase at the pressure and temperature of interest, determined using the standard state thermodynamic terms reported in Table 6 and the EoS data from Table 5. $G_{P,T}^{ex}$ is the excess free energy arising from the second-order tetragonal to orthorhombic phase transition, which can be calculated from:

$$G_{P,T}^{ex} = H_{1,T}^{ex} - TS_{1,298}^{ex} + V_{max}Q_{298}^{2}P \tag{14}$$

where the excess enthalpy and entropy are determined from:

$$H_{1,T}^{ex} = S_{max}\left[T_c^{\circ}\left(Q_{298}^{2} + {}^{1}/_{2}\{Q^{4} - Q_{298}^{4}\}\right) - T_cQ^{2}\right] \tag{15}$$

$$S_{1,T}^{ex} = S_{max}[Q_{298}^{2} - Q^{2}] \tag{16}$$

The standard state Gibbs free energy of formation for the cubic phase at 1 bar and at the temperature of interest, $\Delta_f G_{1,T}^{o}{}^{cubic}$, was calculated from the determined phase boundary conditions using $G_{P,T}^{orth}$ determined from equation 13, with the Landau terms previously reported, and the EoS parameters of the cubic phase (Table 5); i.e.:

$$\Delta_f G_{1,T}^{0}{}^{cubic} = G_{P,T}^{Tet/Orth} - \int_{1\text{ bar}}^{P} V^{cubic}dP. \tag{17}$$

The advantage of using the modified Tait equation of state is that $\int_{1\text{ bar}}^{P} VdP$ can be calculated directly from:

$$PV_0 * \left(1 - a + \left(\frac{a\left((1-bP_{\text{th}})^{1-c} - (1+b(P-P_{\text{th}}))^{1-c}\right)}{b(1-c)P}\right)\right) \tag{18}$$

where the a, b and c parameters are defined in terms of the bulk modulus and its derivative at room pressure (Angel et al. 2014) and the thermal pressure can be calculated according to equation 7, without the need for iteration. In the absence of heat capacity (C_p) data for the cubic phase, we use the same values as for the tetragonal phase, but then refine the first C_p polynomial term (Table 6) along with S and $\Delta_f H$, in a weighted least squares fit to the phase boundary data shown in Figure 7. The resulting orthorhombic to cubic boundary is plotted in Figure 7, which, when compared to the slope of the tetragonal to orthorhombic transition, implies that the orthorhombic phase stability field may pinch out at high temperatures.

The Ru-RuO_2 oxygen buffer

The oxygen fugacity of the Ru + O_2 = RuO_2 buffer can be calculated using the relation:

$$RT \ln fO_2 = \Delta_r G^0_{1\,\mathrm{bar},T} + \int_{1\,\mathrm{bar}}^{P} \Delta V dP. \tag{19}$$

The thermodynamic data for calculating $\Delta_r G^0_{1\,\mathrm{bar},T}$ for the component phases is listed in Table 6 and ΔV is the volume change between RuO_2 and Ru, which can be calculated using data in the same table. A continuous Gibbs free energy is calculated for the tetragonal and orthorhombic phases using equations 13-16, following the methodology of Holland and Powell (1998), although noting that Holland and Powell provide Landau equations for a tricritical transition, whereas the RuO_2 transition, as for stishovite, is second-order.

The only other redox buffers where EoS data allow oxygen fugacities to be reliably determined at pressures > 10 GPa are for the equilibria 2Fe + O_2 = 2FeO (IW) and 2Ni + O_2 = 2NiO (NNO) (Campbell et al., 2009). In Figure 8, oxygen fugacities calculated for the Ru-RuO_2 buffer are normalised against the NNO buffer in order to remove the strong pressure variation. The curve for the equilibrium involving tetragonal and orthorhombic RuO_2 shows that there is no perceptible influence on the fo_2 due to the second-order phase transition, which occurs at ~ 12 GPa at 1273 K. The transition to the cubic phase has a much larger effect on both the slope and the absolute value of the fo_2, which is lower by ~ 0.5 log units at 25 GPa than the value extrapolated for the orthorhombic RuO_2 phase. This difference decreases significantly at high temperature, however, and both values are within 0.2 log units at 2473 K and 25 GPa. In Figure 8, we also make two types of comparisons with extrapolations based on only low pressure data. At 1273 K a dashed curve is calculated

assuming a constant ΔV for the solid phases of the buffering reaction, i.e., ignoring phase transformations and equations of state. The calculated oxygen fugacity is over 1 log unit higher than that determined for the cubic phase at 25 GPa. If, however, the previously available EoS data are employed (compiled by O'Neill and Nell 1997) but the phase transformations are again ignored, as shown by the dashed curve at 2473 K, the resulting oxygen fugacities are still 0.5 log units higher than those calculated for the extrapolated orthorhombic phase. This demonstrates that simultaneous high *P* and *T* EoS data are indeed important for determining accurate oxygen fugacities at pressures approaching those of the lower mantle.

The uncertainties in the determined EoS properties, however, have a relatively small influence on the resulting oxygen fugacities, provided they are approximately of the correct magnitude. K_0 of the cubic RuO_2 phase, for example, would have to change by 40 GPa in order to change the fO_2 of the buffer at 1273 K and 25 GPa by 0.1 log units. An uncertainty of 20% on α_0 also propagates to only 0.1 log units in fO_2 at the same conditions, although it corresponds to volume uncertainties that are ten times larger than those measured.

Propagating all EoS uncertainties over the conditions shown in Figure 8 results in a maximum fO_2 uncertainty of 0.1 log units. We can determine the uncertainties arising from the phase boundary determination of the cubic RuO_2 transformation by changing the boundary gradient. The experimentally determined boundary has a gradient of 390 K GPa^{-1}. If we increase this to 570 K GPa^{-1}, while maintaining approximately the same transition pressure at 298 K, this equates to an uncertainty in the determined pressure of ~ 1 GPa at 1273 K and ~ 1.8 GPa at 2473 K, which is well outside of the experimental uncertainties of 0.3 and 0.5 GPa, respectively. The resulting change in thermodynamic properties determined for the cubic RuO_2 phase propagates to a change in calculated fO_2 at 1273 K and 25 GPa of only 0.06 log units. The same changes in properties result in even smaller shifts in fO_2 at higher temperatures or lower pressures. Thus the maximum uncertainty in fO_2 over the conditions shown in Figure 8 is less than 0.2 log units.

We have parameterised the oxygen fugacity of the Ru-RuO_2 buffer across the stability fields of all three RuO_2 phases using a single polynomial of a similar form to that used by Campbell et al. (2009) i.e.:

$$\log fO_2\,(\text{Ru-RuO}_2) = (a_0 + a_1P + a_2P^2 + a_3P^3) + (b_0 + b_1P + b_2P^2)/T + (c_0 + c_1P)/T^2$$

Using a least squares fitting routine the following parameters were refined,

a_0	a_1	a_2	a_3	b_0	b_1	b_2	c_0	c_1
7.782	-0.00996	0.001932	-3.76×10^{-5}	-13763	592	-3.955	-1.05×10^{6}	-4622

where P is in GPa and T in K. Curves calculated from this parameterisation are shown in Figure 8. The maximum difference with the thermodynamically calculated curves occurs near the orthorhombic to cubic phase transition but is never greater than 0.05 log units over the range of fitted conditions, which cover 773-2773 K and up to 25 GPa. The polynomial becomes rapidly unreliable, however, if extrapolated outside of this range.

Implications

In order to experimentally investigate the stability of ferric iron bearing phases at conditions compatible with the Earth's deep mantle, we require oxygen fugacity buffers that can be mixed directly with experimental samples and undergo minimal chemical interaction other than exchanging oxygen. The Ru-RuO_2 oxygen buffer fulfils this criterion and provides a relatively high oxygen fugacity that should impose relatively high ferric iron contents in mantle phases. However the volumes of both Ru and RuO_2 and any phase transition boundaries need to be accurately known at high pressures and temperatures if oxygen fugacities are to be correctly calculated. We have determined the phase relations and *P-V-T* EoS properties for Ru and RuO_2 phases using in situ X-ray diffraction and additional quench experiments in multi-anvil devices. While no phase transformations were found for Ru metal, RuO_2, which is tetragonal (rutile-structure) at room pressure, undergoes a second-order phase transformation to an orthorhombic $CaCl_2$-structured phase and then a first-order transformation to a cubic (pyrite-type) structured phase. We have used a model based on Landau theory combined with the modified Tait EoS (Holland and Powell 1998) to derive a continuous Gibbs free energy expression for the tetragonal and orthorhombic phases by fitting the second-order phase transition boundary and P-V-T data for both phases. The phase relations for the transition between the orthorhombic and cubic phases were then used along with EoS data for both phases to determine a Gibbs free energy expression for the cubic phase.

The refined gradients for the second- and first-order phase boundaries are 223 K GPa^{-1} and 390 K GPa^{-1}, respectively, which implies that the stability field of the orthorhombic phase pinches out at temperatures >2500 K. A number of studies have emphasized the

importance of RuO_2 transformations as analogues for those encountered by SiO_2 at lower mantle conditions (Haines et al. 1996; 1997; 1998; Haines and Léger 1993; Ming and Magnhani 1982; Ono and Mibe 2011; Ahuja 2001; Rosenblum et al. 1997). While the RuO_2 second-order rutile to $CaCl_2$-type transition is isostructural to that observed for stishovite, the first-order transition to the pyrite structure differs, as SiO_2 first assumes an orthorhombic α PbO_2-type structure above 100 GPa and only assumes the pyrite-type structure above 270 GPa (Kuwayama et al. 2005). In the pyrite-type structure, the Ru cations occupy the corners and the face centers of the unit cell, whereas in the α PbO_2 -type structure, the Ru cations would be required to occupy positions well inside the unit cell. This would likely result in Ru-O bonds that are too short, whereas this is quite possible for the smaller Si cations. For this reason we probably cannot draw conclusions as to the shape of the $CaCl_2$-type stability field for SiO_2 based on our results for RuO_2, because the breakdown transition at high pressure is probably quite different.

It has been proposed that the stishovite second-order transition could create an observable seismic anomaly, or cause scattering of seismic waves in the lower mantle, because the shear modulus goes through a minimum at the transition (Andrault et al. 1998; Carpenter et al. 2000). Although we can place no constraints on this elastic behavior for the RuO_2 phases, we note that the influence of the transition on the volume of RuO_2, while quite strong at room temperature, is predicted by our model to decrease with increasing temperature. This emphasizes the need to support room temperature investigations of the elastic properties across such transitions with high temperature data if conclusions concerning seismic behaviour in the lower mantle are to be drawn.

Using the refined thermodynamic and EoS properties for both Ru and RuO_2 phases, the oxygen fugacity of the buffering assemblage can be calculated reliably to 25 GPa and between 773-2500 K, with an estimated uncertainty of 0.2 log units. A polynomial expression fit to these data provides an accurate description for the oxygen fugacity of the Ru-RuO_2 buffer to conditions at the top of the lower mantle.

Acknowledgements

Raphael Njul and Alex Rother are thanked for sample preparation. Funding was provided within the DFG-SPP program 1833 "Building a Habitable Earth" through grant FR 1555/10-1.

References

Ahuja, R., Rekhi, S., Saxena, S.K., and Johansson, B. (2001) High-pressure structural phase transitions in RuO2 and its geophysical implications. The Journal of Physics and Chemistry of Solids, 62, 2035–2037.

Akins, J.A., and Ahrens, T.J. (2002) Dynamic compression of SiO_2: A new interpretation. Geophysical Research Letters, 29.

Andrault, D., Fiquet, G., Guyot, F., and Hanfland, M. (1998) Pressure-induced landau-type transition in stishovite. Science, 282, 720–724.

Angel, R.J., Alvaro, M., and Gonzalez-Platas, J. (2014) EosFit7c and a Fortran module (library) for equation of state calculations. Zeitschrift für Kristallographie - Crystalline Materials, 229.

Angel, R.J., Alvaro, M., Miletich, R., and Nestola, F. (2017) A simple and generalised P–T–V EoS for continuous phase transitions, implemented in EosFit and applied to quartz. Contributions to Mineralogy and Petrology, 172, 29.

Campbell, A.J., Danielson, L., Righter, K., Seagle, C.T., Wang, Y., and Prakapenka, V.B. (2009) High pressure effects on the iron–iron oxide and nickel–nickel oxide oxygen fugacity buffers. Earth and Planetary Science Letters, 286, 556–564.

Canil, D., and O'Neill, H.S.T.C. (1996) Distribution of Ferric Iron in some Upper-Mantle Assemblages. Journal of Petrology, 37, 609–635.

Carpenter, M.A., Hemley, R.J., and Mao, H.-K. (2000) High-pressure elasticity of stishovite and the P42 / mnm = Pnnm phase transition. Journal of Geophysical Research, 105, 10807–10816.

Chantel, J., Frost, D.J., McCammon, C.A., Jing, Z., and Wang, Y. (2012) Acoustic velocities of pure and iron-bearing magnesium silicate perovskite measured to 25 GPa and 1200 K. Geophysical Research Letters, 39, L19307.

Clendenen, R.L., and Drickamer, H.G. (1964) The effect of pressure on the volume and lattice parameters of ruthenium and iron. The Journal of Physics and Chemistry of Solids, 25, 865–868.

Davis, F.A., and Cottrell, E. (2018) Experimental investigation of basalt and peridotite oxybarometers: Implications for spinel thermodynamic models and Fe^{3+} compatibility during generation of upper mantle melts. The American Mineralogist, 103, 1056–1067.

Dewaele, A., Fiquet, G., Andrault, D., and Hausermann, D. (2000) P-V-T equation of state of periclase from synchrotron radiation measurements. Journal of Geophysical Research, 105, 2869–2877.

Eugster, H.P. (1957) Heterogeneous Reactions Involving Oxidation and Reduction at High Pressures and Temperatures. The Journal of Chemical Physics, 26, 1760–1761.

Fischer, R.A., Campbell, A.J., Chidester, B.A., Reaman, D.M., Thompson, E.C., Pigott, J.S., Prakapenka, V.B., and Smith, J.S. (2018) Equations of state and phase boundary for stishovite and $CaCl_2$-type SiO_2. The American Mineralogist, 103, 792–802.

Frost, D.J, Poe, B.T, Tronnes, R.G., Liebske, C., Duba, A., and Rubie, D.C. (2004) A new large-volume multianvil system. Physics of the Earth and Planetary Interiors, 143-144, 507-514.

Gaillard, F., Scaillet, B., Pichavant, M., and Iacono-Marziano, G. (2015) The redox geodynamics linking basalts and their mantle sources through space and time. Chemical Geology, 418, 217–233.

Gupta, S.D., and Jha, P.K. (2014) Vibrational and elastic properties as a pointer to stishovite to $CaCl_2$ ferroelastic phase transition in RuO_2. Earth and Planetary Science Letters, 401, 31–39.

Haines, J., and Léger, J.M. (1993) Phase transitions in ruthenium dioxide up to 40 GPa: Mechanism for the rutile-to-fluorite phase transformation and a model for the high-pressure behavior of stishovite SiO_2. Physical Review B: Condensed Matter, 48, 13344–13350.

Haines, J., Léger, J.M., and Schulte, O. (1996) Pa3 Modified Fluorite-Type Structures in Metal Dioxides at High Pressure. Science, 271, 629–631.

Haines, J., Leger, J.M., Schulte, O., and Hull, S. (1997) Neutron Diffraction Study of the Ambient-Pressure, Rutile-Type and the High-Pressure, $CaCl_2$-Type Phases of Ruthenium Dioxide. Acta Crystallographica, 53, 880–884.

Haines, J., Leger, J.M., Schmidt, M.W., Petitet, J.P., Pereire, A.S., Da Jornada, J.A.H., and Hull, S. (1998) Structural characterisation of the Pa3 -type, high-pressure phase of ruthenium dioxide. Journal of Physics and Chemistry of Solids, 59, 239–243.

Hazen, R.M., and Finger, L.W. (1981) Bulk moduli and high-pressure crystal structures of rutile-type compounds. The Journal of Physics and Chemistry of Solids, 42, 143–151.

Hirschmann, M.M. (2012) Magma ocean influence on early atmosphere mass and composition. Earth and Planetary Science Letters, 341–344, 48–57.

Hirschmann, M.M., Withers, A.C., Ardia, P., and Foley, N.T. (2012) Solubility of molecular hydrogen in silicate melts and consequences for volatile evolution of terrestrial planets. Earth and Planetary Science Letters, 345-348, 38–48.

Holland, T.J.B., and Powell, R. (1998) An internally consistent thermodynamic data set for phases of petrological interest. Journal of Metamorphic Geology, 16, 309–343.

——— (2011) An improved and extended internally consistent thermodynamic dataset for phases of petrological interest, involving a new equation of state for solids. Journal of Metamorphic Geology, 29, 333–383.

Huang, Y.K., and Chow, C.Y. (2002) The generalized compressibility equation of Tait for dense matter. Journal of Physics D: Applied Physics, 7, 2021.

Ishii, T., Shi, L., Huang, R., Tsujino, N., Druzhbin, D., Myhill, R., Li, Y., Wang, L., Yamamoto, T., Miyajima, N., and others (2016) Generation of pressures over 40 GPa using Kawai-type multi-anvil press with tungsten carbide anvils. The Review of Scientific Instruments, 87, 024501.

Ito, H., Kawada, K., and Akimoto, S. (1974) Thermal expansion of stishovite. Physics of the Earth and Planetary Interiors, 8, 277–281.

Keefner, J.W., Mackwell, S.J., Kohlstedt, D.L., and Heidelbach, F. (2011) Dependence of dislocation creep of dunite on oxygen fugacity: Implications for viscosity variations in Earth's mantle. Journal of Geophysical Research, 116, 1.

Kiseeva, E.S., Vasiukov, D.M., Wood, B.J., McCammon, C., Stachel, T., Bykov, M., Bykova, E., Chumakov, A., Cerantola, V., Harris, J.W., and others (2018) Oxidized iron in garnets from the mantle transition zone. Nature Geoscience, 11, 144–147.

Kuwayama, Y., Hirose, K., Sata, N., and Ohishi, Y. (2005) The pyrite-type high-pressure form of silica. Science, 309, 923–925.

Larson, A.C., and Von Dreele, R.B. (2004) General Structure Analysis System (GSAS). Los Alamos National Laboratory.

Lauterbach, S., McCammon, C.A., van Aken, P., Langenhorst, F., and Seifert, F. (2000) Mössbauer and ELNES spectroscopy of (Mg,Fe)(Si,Al)O_3 perovskite: a highly oxidised component of the lower mantle. Contributions to Mineralogy and Petrology, 138, 17–26.

Lugovskoy, A.V., Belov, M.P., Krasilnikov, O.M., and Vekilov, Y.K. (2014) Stability of the hcp Ruthenium at high pressures from first principles. Journal of Applied Physics, 116, 103507.

Lundin, U., Fast, L., Nordström, L., Johansson, B., Wills, J.M., and Eriksson, O. (1998) Transition-metal dioxides with a bulk modulus comparable to diamond. Physical Review B: Condensed Matter, 57, 4979–4982.

Matjuschkin, V., Brooker, R.A., Tattitch, B., Blundy, J.D., and Stamper, C.C. (2015) Control and monitoring of oxygen fugacity in piston cylinder experiments. Contributions to Mineralogy and Petrology, 169, 9.

Millot, M., Dubrovinskaia, N., Blaha, S., Dubrovinsky, L., Braun, D.G., Celliers, P.M., Collins, G.W., Eggert, J.H., and Jeanloz, R. (2015) Shock compression of stishovite and melting of silica at planetary interior conditions. Science, 347, 418–420.

Ming, L.C., and Manghnani, M.H. (1982) High-Pressure Phase Transformations in Rutile-Structured Dioxides. In S. Akimoto and M.H. Manghnani, Eds., High-Pressure Research in Geophysics pp. 329–360. Center for Academic Publications, Tokyo.

O'Neill, H.S.C., and Nell, J. (1997) Gibbs free energies of formation of RuO_2, IrO_2, and OsO_2: A high-temperature electrochemical and calorimetric study. Geochimica et Cosmochimica Acta, 61, 5279–5293.

O'Neill, H.S.C., Berry, A.J., McCammon, C.C., Jayasuriya, K.D., Campbell, S.J., and Foran, G. (2006) An experimental determination of the effect of pressure on the $Fe^{3+}/\sum Fe$ ratio of an anhydrous silicate melt to 3.0 GPa. The American Mineralogist, 91, 404–412.

Ono, S., and Mibe, K. (2011) Determination of the phase boundary of the ferroelastic rutile to $CaCl_2$ transition in RuO_2 using in situ high-pressure and high-temperature Raman spectroscopy. Physical Review B: Condensed Matter, 84, 054114.

Pommier, A., Gaillard, F., and Pichavant, M. (2010) Time-dependent changes of the electrical conductivity of basaltic melts with redox state. Geochimica et Cosmochimica Acta, 74, 1653–1671.

Rao, K.V.K., and Iyengar, L. (1969) X-ray studies on the thermal expansion of ruthenium dioxide. Acta Crystallographica Section A: Foundations of Crystallography, 25, 302–303.

Righter, K., Campbell, A.J., Humayun, M., and Hervig, R.L. (2004) Partitioning of Ru, Rh, Pd, Re, Ir, and Au between Cr-bearing spinel, olivine, pyroxene and silicate melts. Geochimica et Cosmochimica Acta, 68, 867–880.

Rohrbach, A., Ballhaus, C., Golla-Schindler, U., Ulmer, P., Kamenetsky, V.S., and Kuzmin, D.V. (2007) Metal saturation in the upper mantle. Nature, 449, 456–458.

Rosenblum, S.S., Weber, W.H., and Chamberland, B.L. (1997) Raman-scattering observation of the rutile-to-CaCl2 phase transition in RuO2. Physical Review B: Condensed Matter and Materials Physics, 56, 529–533.

Schroeder, R.H., Schmitz-Pranghe, N., and Kohlhaas, R. (1972) Experimentelle Bestimmung der Gitterparameter der Platinmetalle im Temperaturbereich von -190 bis 1709°C. Zeitschrift Metallkunde, 63, 12–16.

Smith, E.M., Shirey, S.B., Nestola, F., Bullock, E.S., Wang, J., Richardson, S.H., and Wang, W. (2016) Large gem diamonds from metallic liquid in Earth's deep mantle. Science, 354, 1403–1405.

Smyth, J.R., Bolfan-Casanova, N., Avignant, D., El-Ghozzi, M., and Hirner, S.M. (2014) Tetrahedral ferric iron in oxidized hydrous wadsleyite. The American Mineralogist, 99, 458–466.

Stagno, V., Tange, Y., Miyajima, N., McCammon, C.A., Irifune, T., and Frost, D.J. (2011) The stability of magnesite in the transition zone and the lower mantle as function of oxygen fugacity. Geophysical Research Letters, 38.

Tao, R., Fei, Y., Bullock, E.S., Xu, C., and Zhang, L. (2018) Experimental investigation of Fe^{3+}-rich majoritic garnet and its effect on majorite geobarometer. Geochimica et Cosmochimica Acta, 225, 1–16.

Toby, B.H. (2001) EXPGUI a graphical user interface for GSAS. Journal of Applied Crystallography, 34, 210–213.

Tse, J.S., Klug, D.D., Uehara, K., Li, Z.Q., Haines, J., and Léger, J.M. (2000) Elastic properties of potential superhard phases of RuO_2. Physical Review B: Condensed Matter, 61, 10029–10034.

Tsuchiya, T. (2003) First-principles prediction of the P-V-T equation of state of gold and the 660-km discontinuity in Earth's mantle. Journal of Geophysical Research, 108, 2462.

Tsuchiya, T., Caracas, R., and Tsuchiya, J. (2004) First principles determination of the phase boundaries of high-pressure polymorphs of silica. Geophysical Research Letters, 31.

Wang, Y., Rivers, M., Sutton, S., Nishiyama, N., Uchida, T., and Sanehira, T. (2009) The large-volume high-pressure facility at GSECARS: A "Swiss-army-knife" approach to synchrotron-based experimental studies. Physics of the Earth and Planetary Interiors, 174, 270–281.

Woodland, A.B., and O'Neill, H.S.C. (1997) Thermodynamic data for Fe-bearing phases obtained using noble metal alloys as redox sensors. Geochimica et Cosmochimica Acta, 61, 4359–4366.

Woodland, A.B., Kornprobst, J., and Tabit, A. (2006) Ferric iron in orogenic lherzolite massifs and controls of oxygen fugacity in the upper mantle. Lithos, 89, 222–241.

Yang, R., and Wu, Z. (2014) Elastic properties of stishovite and the $CaCl_2$-type silica at the mantle temperature and pressure: An ab initio investigation. Earth and planetary science letters, 404, 14–21.

Yoshino, T., and Katsura, T. (2013) Electrical Conductivity of Mantle Minerals: Role of Water in Conductivity Anomalies. Annual Review of Earth and Planetary Sciences, 41, 605–628.

Zhang, H.L., Hirschmann, M.M., Cottrell, E., and Withers, A.C. (2017) Effect of pressure on $Fe^{3+}/\Sigma Fe$ ratio in a mafic magma and consequences for magma ocean redox gradients. Geochimica et Cosmochimica Acta, 204, 83–103.

Table 1. In situ experimental pressure and temperature conditions determined from the unit-cell *a*-axis parameters of Au and MgO.

Run #	Au *a*-axis (Å)	MgO *a*-axis (Å)	*P* Au (GPa)	*P* MgO (GPa)	*T* (K)
T2135.001	4.0812 (2)	4.2116 (2)	0.00010 (1)	0.00010 (1)	298
T2135.003*	4.0250 (2)	4.1546 (5)	7.9	7.8	
T2135.004	4.0773 (3)	4.2024 (3)	7.4	7.0	1273
T2135.006	4.0684 (3)	4.1944 (2)	7.2	6.7	1073
T2135.009	4.0569 (2)	4.1851 (3)	6.7	6.0	773
T2135.012	4.0455 (2)	4.1762 (3)	4.8	4.3	298
T2135.014*	4.0210 (2)	4.1524 (3)	8.6	7.5	298
T2135.015	4.0578 (3)	4.1841 (4)	9.9	9.3	1273
T2135.017	4.0536 (2)	4.1796 (2)	9.2	8.6	1073
T2135.019	4.0434 (3)	4.1691 (2)	8.5	8.1	773
T2135.022	4.0302 (4)	4.1578 (5)	7.1	6.7	298
T2135.023*	4.0133 (3)	4.1404 (3)	9.8	9.1	298
T2135.025	4.0425 (3)	4.1705 (5)	12.0	11.0	1273
T2135.026	4.0342 (3)	4.1580 (7)	11.9	11.4	1073
T2135.029	4.0249 (2)	4.1537 (5)	11.3	10.1	773
T2135.030	4.0161 (3)	4.1410 (5)	9.4	9.1	298
T2135.032*	3.9968 (3)	4.1231 (5)	12.7	11.7	298
T2135.034	4.0238 (3)	4.1439 (2)	13.5	13.4	1073
T2135.036	4.0150 (2)	4.1348 (2)	12.9	12.8	773
T2135.038	4.0045 (2)	4.1228 (2)	11.3	11.7	298
T2140.001	4.0788 (2)	4.2122 (2)	0.0001	0.0001	298
T2140.003*	3.9601 (6)	4.0876 (7)	19.3	17.3	298
T2140.004	4.0256 (4)	4.1487 (4)	15.4	15.3	1473
T2140.007	4.0219 (3)	4.1447 (4)	14.7	14.6	1273
T2140.008	4.0178 (3)	4.1390 (4)	14.1	14.1	1073
T2140.011	4.0081 (3)	4.1286 (6)	13.6	13.8	773
T2140.012	3.9995 (2)	4.1218 (5)	11.8	11.9	298
T2140.014*	3.9910 (2)	4.1121 (3)	13.3	13.4	298
T2140.015	4.0181 (3)	4.1382 (7)	16.5	16.8	1473
T2140.018	4.0124 (3)	4.1345 (2)	16.3	16.0	1273
T2140.019	4.0077 (3)	4.1304 (3)	15.8	15.4	1073
T2140.022	4.0015 (2)	4.1233 (3)	14.8	14.6	773
T2140.023	3.9944 (3)	4.1145 (3)	12.7	13.1	298
T2140.025*	3.9776 (2)	4.1009 (2)	15.8	15.2	298
T2140.026	4.0080 (3)	4.1253 (2)	18.2	18.7	1473
T2140.029	4.0008 (2)	4.1207 (3)	18.2	18.1	1273
T2140.030	3.9964 (2)	4.1182 (4)	17.7	17.2	1073
T2140.033	3.9899 (4)	4.1040 (5)	16.8	17.5	773
T2140.034	3.9831 (3)	4.0996 (3)	14.8	15.4	298

*Data point obtained after increasing pressure at room temperature. At these conditions data for the Ru/RuO_2 sample were not collected. Pressure values have been calculated using the *P*-*V*-*T* equations of state for Au (Tsuchiya 2003) and MgO (Dewaele et al. 2000). The pressure

uncertainties are approximately ±0.3 GPa. Temperatures have been measured with a thermocouple with an estimated uncertainty of ±40 K due to the thermal gradient over the diffraction volume.

Table 2. Unit-cell lattice parameters of ruthenium metal

Run #	*P* Au (GPa)	*T* (K)	*a* (Å)	*c* (Å)	*V* (Å3)
T2135.001	0.0001 (0)	298	2.708 (3)	4.280 (6)	27.18 (5)
T2135.004	7.4 (0.2)	1273	2.704 (3)	4.285 (14)	27.12 (8)
T2135.006	7.2 (0.2)	1073	2.701 (3)	4.283 (8)	27.04 (5)
T2135.009	6.7 (0.2)	773	2.697 (3)	4.274 (6)	26.93 (5)
T2135.012	4.8 (0.1)	298	2.694 (2)	4.260 (6)	26.77 (4)
T2135.015	9.9 (0.2)	1273	2.697 (2)	4.272 (11)	26.91 (6)
T2135.017	9.2 (0.2)	1073	2.696 (5)	4.270 (12)	26.88 (9)
T2135.019	8.5 (0.3)	773	2.693 (3)	4.266 (8)	26.78 (6)
T2135.022	7.1 (0.1)	298	2.687 (4)	4.256 (5)	26.62 (4)
T2135.025	12.0 (0.2)	1273	2.686 (3)	4.287 (3)	26.78(14)
T2135.026	11.9 (0.2)	1073	2.686 (2)	4.267 (10)	26.65 (5)
T2135.029	11.3 (0.2)	773	2.684 (3)	4.253 (6)	26.53 (5)
T2135.030	9.4 (0.1)	298	2.680 (2)	4.248 (8)	26.42 (5)
T2135.034	13.5 (0.2)	1073	2.681 (2)	4.254 (10)	26.47 (6)
T2135.036	12.9 (0.2)	773	2.677 (2)	4.254 (7)	26.41 (5)
T2135.038	11.3 (0.1)	298	2.674 (2)	4.244 (7)	26.28 (5)
T2140.001	0.0001 (0)	298	2.707 (2)	4.280 (4)	27.17 (3)
T2140.004	15.4 (0.2)	1473	2.681 (2)	4.263 (4)	26.54 (3)
T2140.007	14.7 (0.2)	1273	2.683 (2)	4.256 (13)	26.47 (8)
T2140.008	14.1 (0.2)	1073	2.681 (3)	4.250 (8)	26.40 (5)
T2140.011	13.6 (0.3)	773	2.677 (2)	4.248 (9)	26.32 (6)
T2140.012	11.8 (0.1)	298	2.673 (2)	4.235 (7)	26.19 (5)
T2140.015	16.5 (0.2)	1473	2.677 (2)	4.259 (7)	26.43 (5)
T2140.018	16.3 (0.2)	1273	2.675 (2)	4.2505 (3)	26.33 (15)
T2140.019	15.8 (0.2)	1073	2.675 (2)	4.249 (9)	26.31 (5)
T2140.022	14.8 (0.2)	773	2.673 (2)	4.238 (6)	26.20 (4)
T2140.023	12.7 (0.1)	298	2.669 (2)	4.231 (5)	26.10 (3)
T2140.026	18.2 (0.2)	1473	2.672 (3)	4.253 (14)	26.29 (8)
T2140.029	18.2 (0.2)	1273	2.671 (4)	4.248 (13)	26.24 (7)
T2140.030	17.7 (0.2)	1073	2.670 (3)	4.230 (9)	26.10 (6)
T2140.033	16.8 (0.3)	773	2.669 (2)	4.230 (5)	26.08 (3)
T2140.034	14.8 (0.1)	298	2.664 (4)	4.223 (20)	25.98 (11)

Table 3. Unit-cell lattice parameters of ruthenium dioxide.

Run #	*P* Au (GPa)	*T* (K)	*a* (Å)	*b* (Å)	*c* (Å)	*V* (Å³)	phase
T2135.001	0.0001	298	4.4993 (3)		3.1067 (3)	62.889 (8)	tetr
T2135.004	7.4 (0.2)	1273	4.5020 (4)		3.0753 (4)	62.330 (10)	tetr
T2135.006	7.2 (0.2)	1073	4.4883 (3)		3.0806 (3)	62.056 (8)	tetr
T2135.009	6.7 (0.2)	773	4.4764 (4)		3.0870 (4)	61.858 (9)	tetr
T2135.012	4.8 (0.1)	298	4.4646 (4)		3.1000 (4)	61.791 (12)	tetr
T2135.015	9.9 (0.2)	1273	4.4848 (4)		3.0730 (4)	61.808 (11)	tetr
T2135.017	9.2 (0.2)	1073	4.4788 (4)		3.0770 (4)	61.723 (9)	tetr
T2135.019	8.5 (0.3)	773	4.4668 (4)		3.0834 (4)	61.522 (9)	tetr
T2135.022	7.1 (0.1)	298	4.4569 (4)		3.0889 (4)	61.357 (9)	tetr
T2135.025	12.0 (0.2)	1273	4.5685 (7)	4.3666 (9)	3.0700 (4)	61.243 (13)	ortho
T2135.026	11.9 (0.2)	1073	4.5553 (6)	4.3588 (8)	3.0732 (5)	61.021 (10)	ortho
T2135.029	11.3 (0.2)	773	4.5467 (7)	4.3499 (9)	3.0763 (5)	60.842 (11)	ortho
T2135.030	9.4 (0.1)	298	4.4726 (8)	4.3850 (10)	3.0866 (5)	60.535 (14)	ortho
T2135.034	13.5 (0.2)	1073	4.5760 (8)	4.3047 (8)	3.0618 (6)	60.313 (12)	ortho
T2135.036	12.9 (0.2)	773	4.5616 (9)	4.2900 (7)	3.0703 (5)	60.082 (12)	ortho
T2135.038	11.3 (0.1)	298	4.5376 (14)	4.2901 (9)	3.0736 (6)	59.833 (14)	ortho
T2140.001	0.0001	298	4.4977 (2)		3.1081 (2)	62.875 (7)	tetr
T2140.004	15.4 (0.2)	1473	4.8217 (2)			112.100 (16)	cubic
T2140.007	14.7 (0.2)	1273	4.8164 (2)			111.727 (14)	cubic
T2140.008	14.1 (0.2)	1073	4.8110 (2)			111.351 (12)	cubic
T2140.011	13.6 (0.3)	773	4.8046 (2)			110.912 (12)	cubic
T2140.012	11.8 (0.1)	298	4.7976 (2)			110.423 (12)	cubic
T2140.015	16.5 (0.2)	1473	4.8165 (2)			111.734 (12)	cubic
T2140.018	16.3 (0.2)	1273	4.8077 (2)			111.127 (14)	cubic
T2140.019	15.8 (0.2)	1073	4.8044 (2)			110.904 (13)	cubic
T2140.022	14.8 (0.2)	773	4.7984 (2)			110.485 (11)	cubic
T2140.023	12.7 (0.1)	298	4.7918 (2)			110.025 (11)	cubic
T2140.026	18.2 (0.2)	1473	4.8059 (2)			111.003 (14)	cubic
T2140.029	18.2 (0.2)	1273	4.7994 (2)			110.550 (15)	cubic
T2140.030	17.7 (0.2)	1073	4.7944 (2)			110.207 (14)	cubic
T2140.033	16.8 (0.3)	773	4.7878 (2)			109.756 (12)	cubic
T2140.034	14.8 (0.1)	298	4.7822 (2)			109.369 (16)	cubic

Tetr=tetragonal; ortho=orthorhombic

Table 4. Experimental conditions and resulting RuO_2 phases from multi-anvil quench experiments. Pressure and temperature uncertainties are estimated to be on the order of 0.5 GPa and 100 K respectively.

Run #	*P* (GPa)	*T* (K)	Duration (min)	RuO_2 product
S6973	4	1873	20	Tetragonal
S6928	4	1673	15	Tetragonal
S6820	6	2023	10	Tetragonal
S6889	6	2023	15	Tetragonal
S6811	6	2173	5	Tetragonal
S6879	6	2173	15	Tetragonal
S6977	8	2173	30	Tetragonal
S6777	8	2173	30	Tetragonal
Z1791	10	2173	15	Tetragonal
S6510	10	2173	30	Tetragonal
Z1468	15	2373	45	Tetragonal
Z1621	17	2473	10	Tetragonal
Z1666	18	2473	10	Cubic
S6654	20	2473	5	Cubic
S6606	23	2573	5	Cubic
S6776	23	2573	10	Cubic

Table 5. *P-V-T* Equation of state parameters

Phase	V_0 (Å^3)	K_0 (GPa)	$\partial K_T/\partial T$	θ (K)	α_0 (x10^{-5})	α_1 (x10^{-8})
Ru Metal	27.185 (4)	304 (2)	-0.052 (4)		2.09 (28)	0.85 (24)
RuO_2						
Tetragonal	62.89 (5)	261 (4)		487	1.57 (7)	
Cubic	114.9 (2)	269 (12)		513	2.15 (6)	
Landau terms	V_{max} = 0.0253 (Jbar^{-1})	S_{max} = 1.14 (JK^{-1})	T_c^o = -1413 (K)			

Note: θ, the Einstein temperature, was estimated from the molar entropy, as described in the text. α_0 and α_1 have units K^{-1} and K^{-2} respectively.

Table 6. Molar thermodynamic properties for calculating the fo_2 for the Ru-RuO_2 buffer

Phase	S	$\Delta_f H$	V_0	Cp (J K^{-1}) terms			
	(JK^{-1})	(kJ)	(J bar^{-1})	*a*	*b*	*c*	*d*
RuO_2 (tetrag)	46.15	-314.13	1.856*§	119.277	0.000626	-105800	-1074.6
RuO_2 (cubic)	41.99*	-299.67*	1.730*	121.577*	0.000626	-105800	-1074.6
Ru	28.5			13.054	0.010052	-345700	205.2
O_2	205.15			47.255	-0.00046	440200	-393.5

Notes: The *Cp* equation is $a+bT+cT^{-2}+dT^{-0.5}$. The * indicates values refined in this study, whereas all other data were either determined or compiled by O'Neill and Nell (1997). § the volume is lower than the measured value due to the contribution from $V_{P,T}^{ex}$ through equation (12).

Figure 1: (Top) schematic of the experimental assembly used in the multi-anvil press. Pellets of sample material and pressure calibrant, 1.7 mm in diameter and approx. 1 mm thick were stacked vertically in a 10-mm edge-length octahedral pressure medium (see text), separated by alumina discs. The sample was heated with a Re foil furnace with laser cut windows to allow the passage of the X-ray beam (inset image). (Bottom) BSE image of a recovered run product, showing pressure calibrant, sample, furnace and thermocouple. The image has been composed from several different brightness settings to better show all details.

Figure 2: Schematic of the setup used to collect X-ray diffraction data of Ru and RuO_2 at the beam line 13-ID-D of the Advanced Photon Source.

Figure 3: Pressure-temperature paths of in situ X-ray diffraction experiments T2135 (green) and T2140 (blue). Pressures were calculated using the *P-V-T* EoS of Au. Empty symbols indicate conditions where x-ray diffraction was collected only from the pressure markers. The pressure was increased after each cycle of heating. In experiment T2140 the pressure was first increased to ~19 GPa but dropped significantly, at constant press load, during heating, most likely due to the large volume change as cubic RuO_2 was formed.

Figure 4: Examples of energy dispersive diffraction patterns collected for Ru/RuO_2 samples at different pressures and temperatures. Dotted red curves: observed intensity data; black solid curves: results from Le Bail fits (calculated intensities + background). The reflection positions for the Ru (green) and RuO_2 (blue) phases are shown as vertical ticks. Fluorescence peaks at ~85 and ~88 keV have been ignored during Le Bail fitting.

Figure 5: *P-V-T* data collected for ruthenium metal at different pressures and temperatures. The data of the different experiments have been normalized with respect their measured room pressure values and have been here reported with V_0 normalized to 27.185 Å^3. Curves show the resulting EoS fits obtained using the modified Tait equation and a two-term polynomial expression for the thermal expansion. The room pressure compression V/V_0 data of Clendenen & Drickamer (1967; triangles) reported with V_0 normalized to 27.185 Å^3 are shown for comparison.

Figure 6: *P-V-T* compression data for the tetragonal (diamonds) orthorhombic (squares) and cubic (circles) phases of RuO_2. Curves show the fit of the equations of state which account for the effect of the second-order tetragonal to orthorhombic phase transition modelled using Landau theory. Results of single crystal compression experiments by Hazen and Finger (1981; small diamonds) and room pressure thermal expansion measurements to 975 K (Rao and Iyengar 1969) are also shown and were included in the fitting procedure.

Figure 7: Phase relations of RuO_2 as a function of *P* and *T*. Larger symbols indicate individual in situ XRD analyses from this study, open symbols show the results from quench experiments at higher temperatures and small symbols show the in situ results of Ono & Mibe (2011) for the tetragonal-orthorhombic transition, the only other reported study on this transition. Darker red symbols for the cubic phase indicate conditions where the data are not employed to determine the orthorhombic-cubic phase boundary due to lower temperatures

and, hence, potential metastability. The black lines show the fit of thermodynamic models for both transitions as described in the text.

Figure 8: The log fO_2 for the $Ru+O_2 \leftrightarrow RuO_2$ buffering equilibrium at 1273 K and 2473 K calculated for the three RuO_2 polymorphs as a function of pressure and normalized to the oxygen fugacity of the nickel-nickel oxide (NNO) buffer (Campbell et al., 2009). The black curves show the polynomial parameterizations, which predict the logfo_2 for the Ru-RuO_2 buffer to within 0.05 of a log unit over this pressure and temperature range. For comparison, the dashed grey curve at 1273 K shows the extrapolated fo_2 assuming a constant room *P* and *T* volume change for the buffering reaction, whereas the dashed grey curve at 2473 K shows the fo_2 calculated using the previous EoS parameters summarized by O'Neill and Nell (1997). Both extrapolations ignore the occurrence of RuO_2 phase transitions.

This is a preprint, the final version is subject to change, of the American Mineralogist (MSA)
Cite as Authors (Year) Title. American Mineralogist, in press.
DOI: https://doi.org/10.2138/am-2020-7060

Figure 1

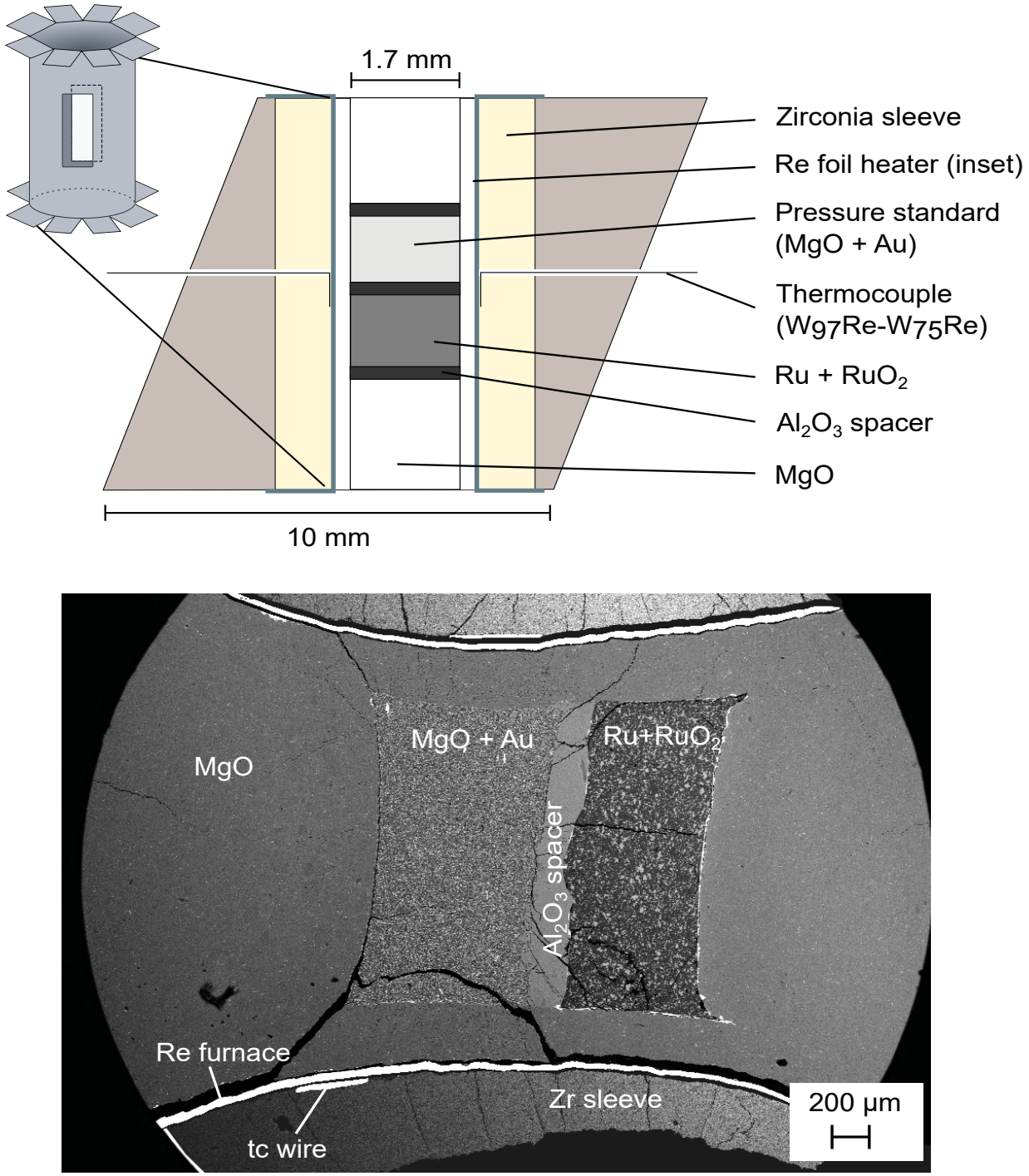

This is a preprint, the final version is subject to change, of the American Mineralogist (MSA)
Cite as Authors (Year) Title. American Mineralogist, in press.
DOI: https://doi.org/10.2138/am-2020-7060

Figure 2

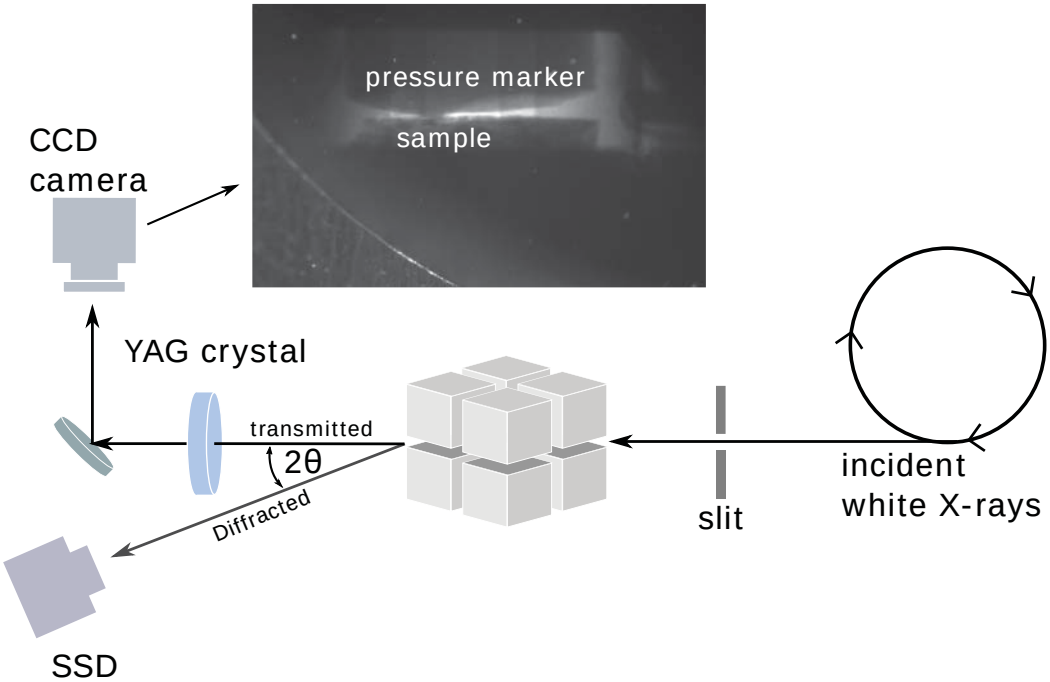

This is a preprint, the final version is subject to change, of the American Mineralogist (MSA)
Cite as Authors (Year) Title. American Mineralogist, in press.
DOI: https://doi.org/10.2138/am-2020-7060

Figure 3

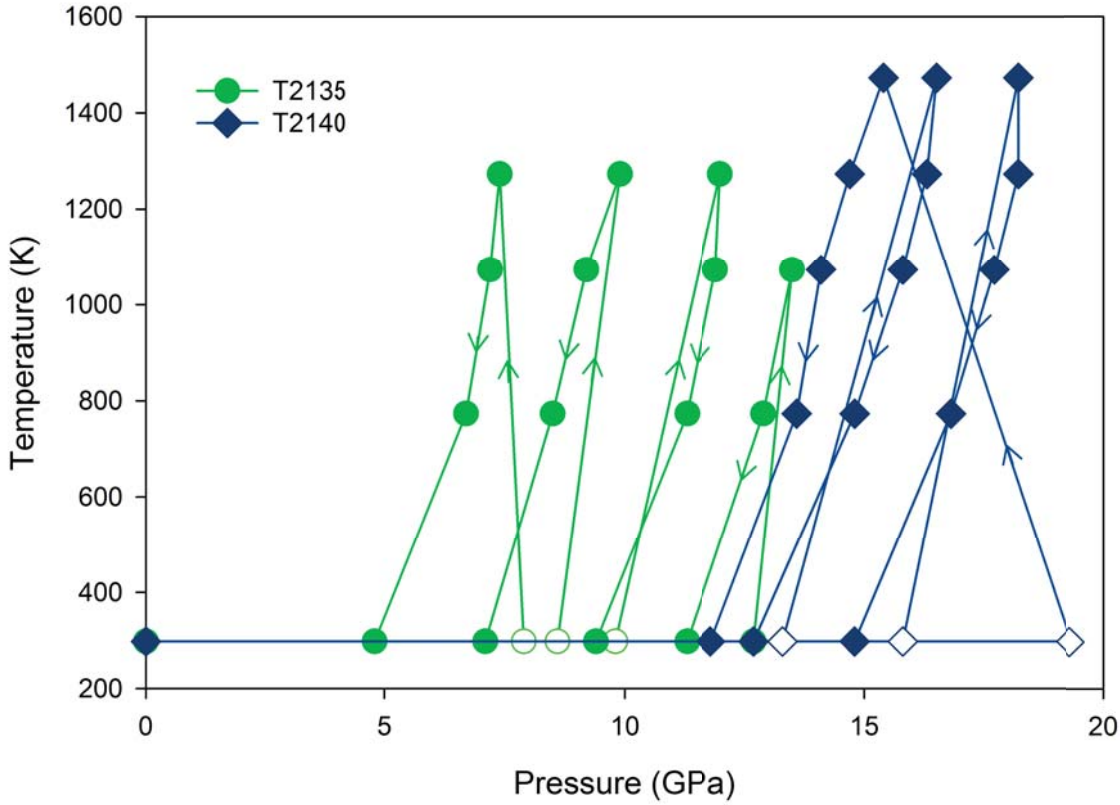

This is a preprint, the final version is subject to change, of the American Mineralogist (MSA)
Cite as Authors (Year) Title. American Mineralogist, in press.
DOI: https://doi.org/10.2138/am-2020-7060

Figure 4

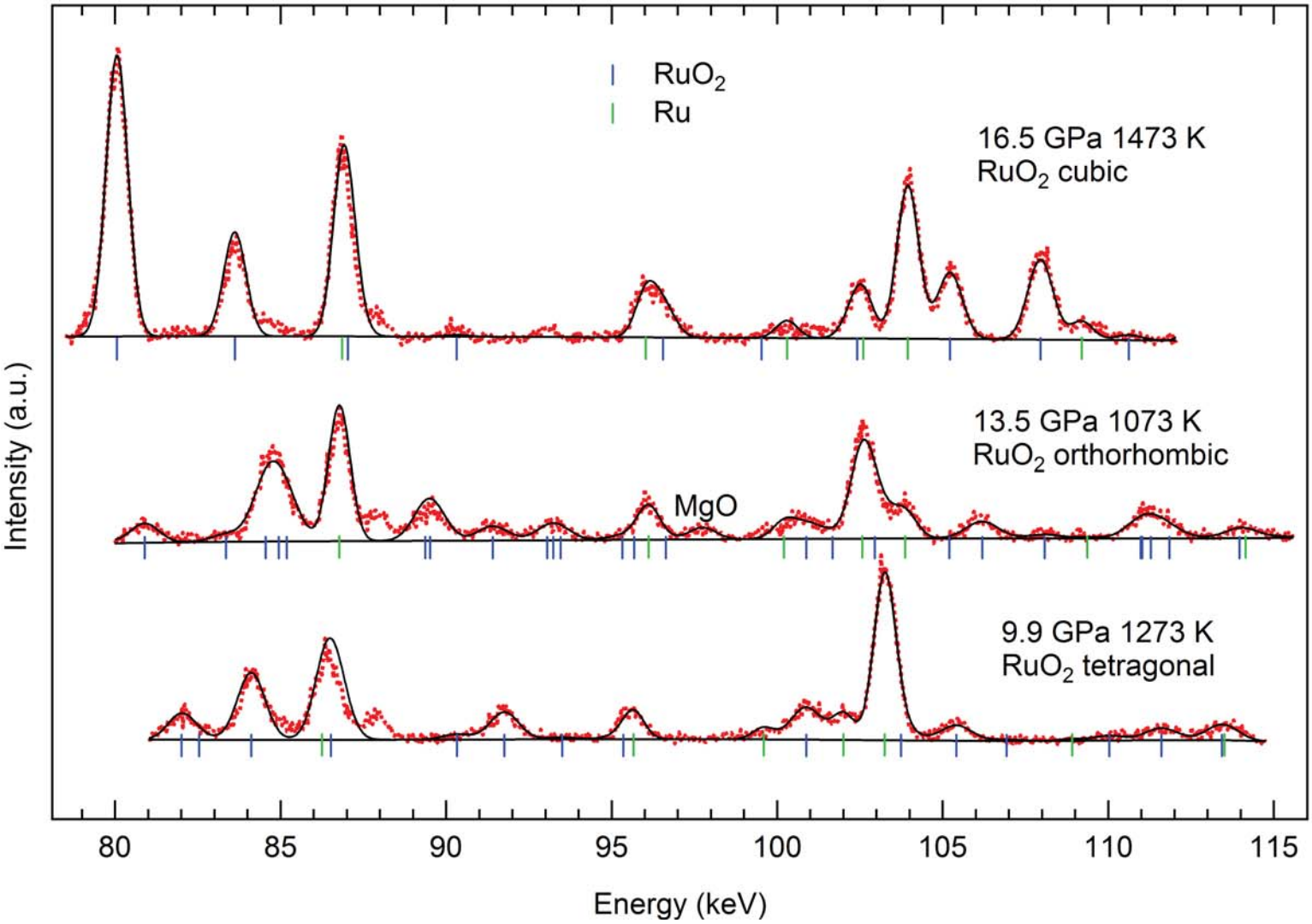

This is a preprint, the final version is subject to change, of the American Mineralogist (MSA)
Cite as Authors (Year) Title. American Mineralogist, in press.
DOI: https://doi.org/10.2138/am-2020-7060

Figure 5

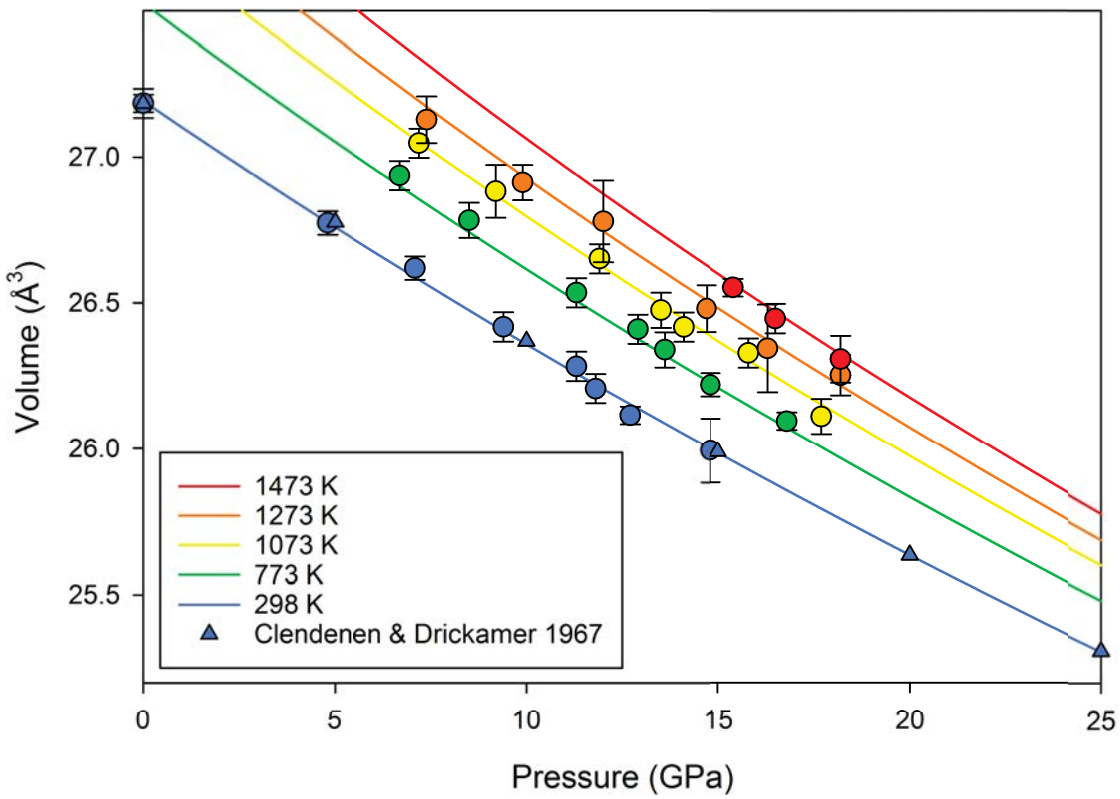

Figure 6

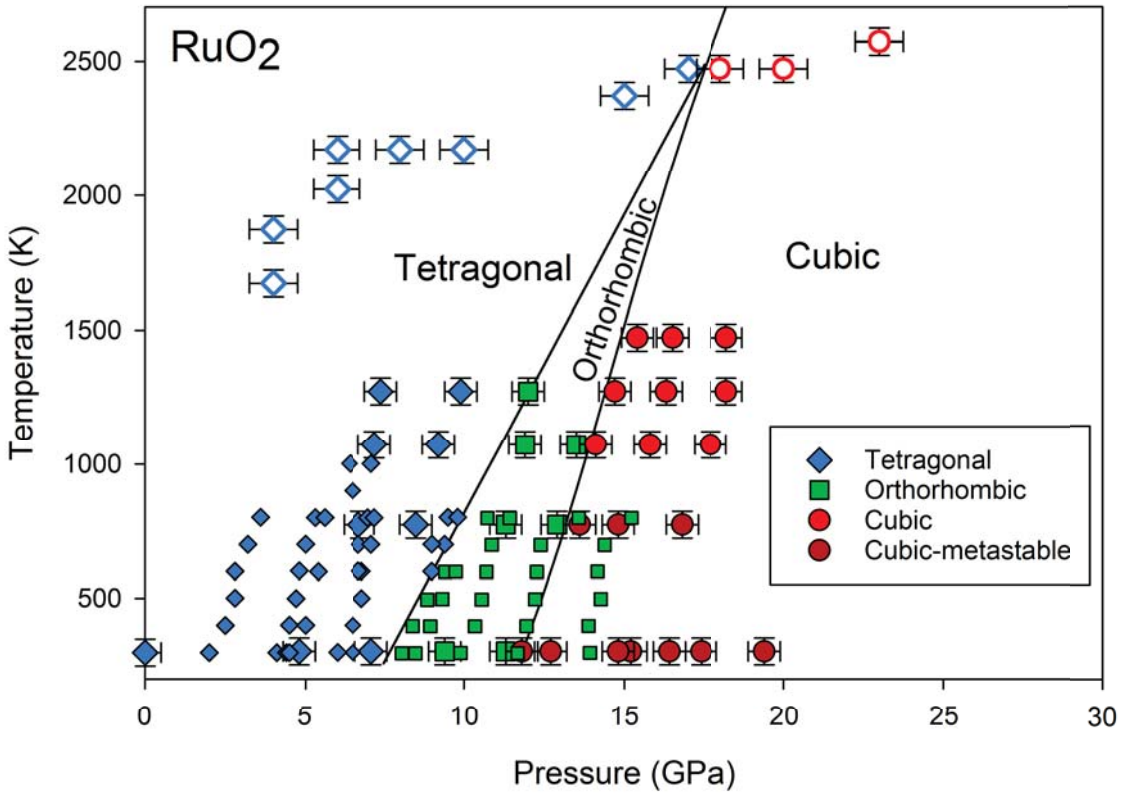
RuO2
Tetragonal
Orthorhombic
Cubic
Tetragonal
Orthorhombic
Cubic
Cubic-metastable
Temperature (K)
Pressure (GPa)
2500
2000
1500
1000
500
0
5
10
15
20
25
30

Figure 7

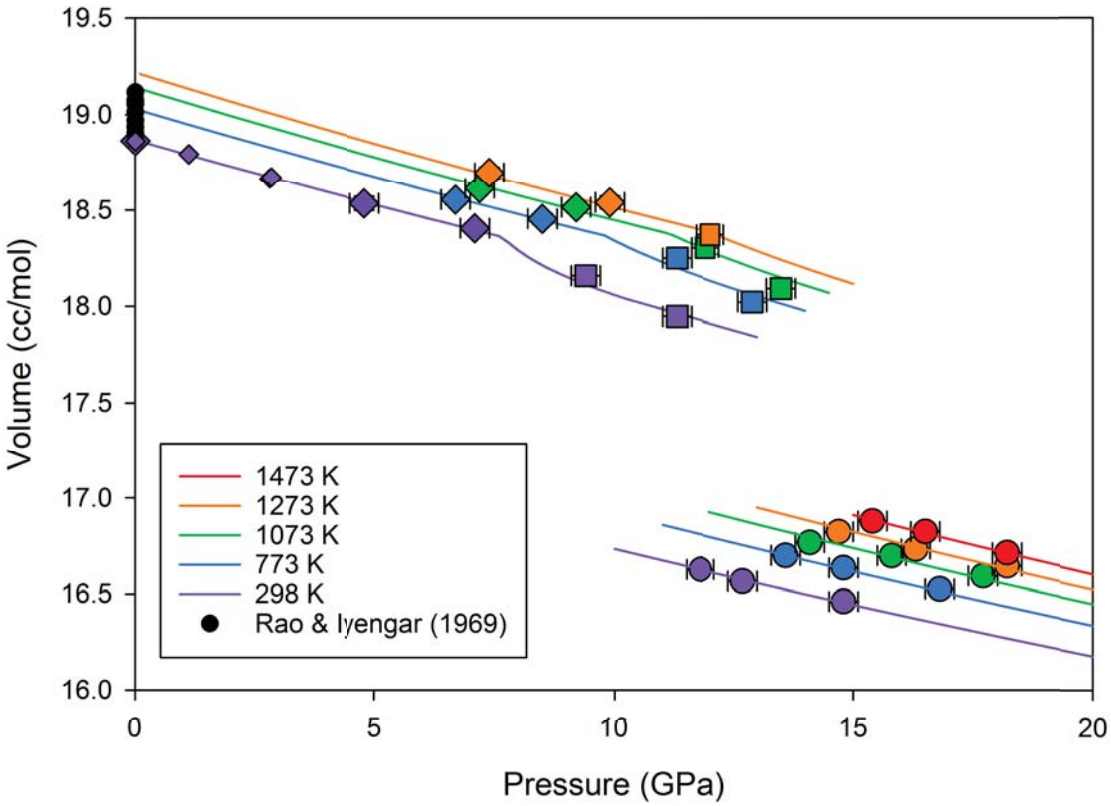
19.5
19.0
18.5
18.0
17.5
17.0
16.5
16.0
Volume (cc/mol)
0
5
10
15
20
Pressure (GPa)
1473 K
1273 K
1073 K
773 K
298 K
Rao & Iyengar (1969)

Figure 8

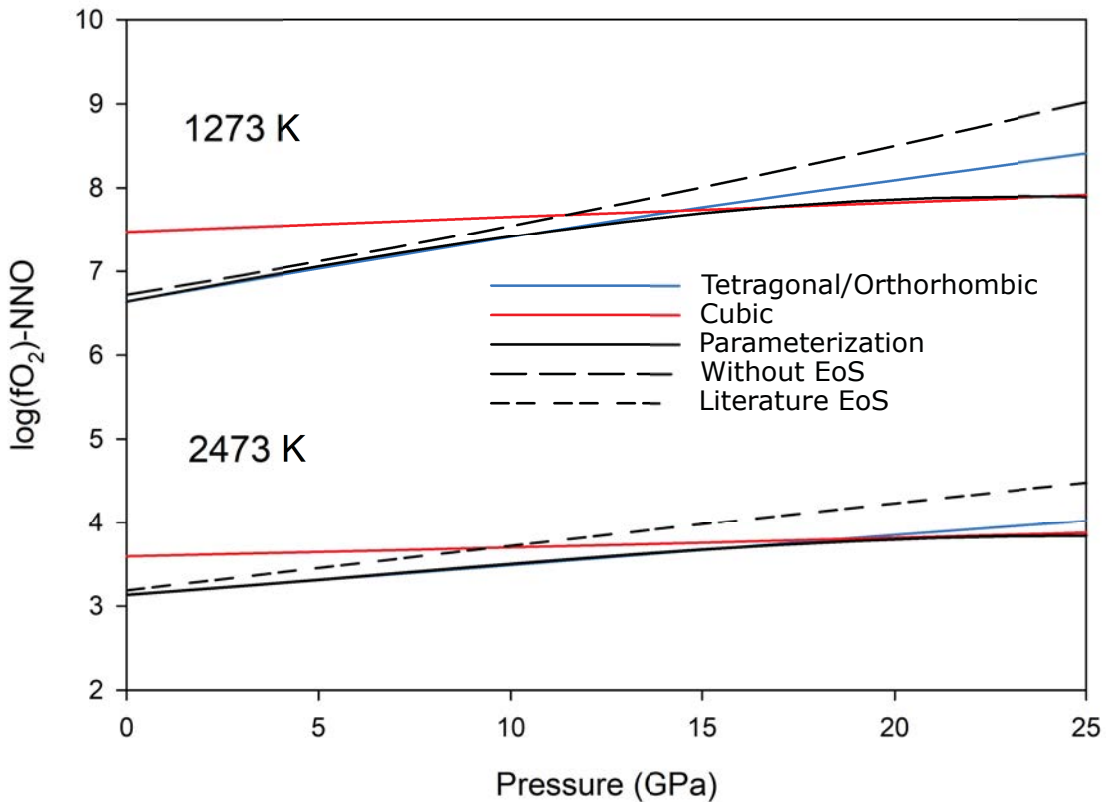
1273 K
2473 K
Tetragonal/Orthorhombic
Cubic
Parameterization
Without EoS
Literature EoS
log(fO2)-NNO
Pressure (GPa)
10
9
8
7
6
5
4
3
2
0
5
10
15
20
25